THE JOURNAL OF PHYSICAL CHEMISTRY C
A JOURNAL OF THE AMERICAN CHEMICAL SOCIETY

pubs.acs.org/JPCC
Article

Assessing Low-Cost Computational Methods against Structural Properties and Size Effects of Pt nanoparticles

Alberto Ricchebuono,* Eleonora Vottero, Andrea Piovano, Elena Groppo, Pascal Raybaud, and Céline Chizallet*

Cite This: J. Phys. Chem. C 2023, 127, 18454−18465

ABSTRACT: An evaluation of the performances of several known low-cost methods for the reproduction of structural features of differently sized Pt nanoparticles (NPs) is presented. The full density functional theory PBE-dDsC functional (within the plane-wave formalism) was employed to benchmark the semiempirical tight-binding DFTB and GFN*n*-xTB (n = 0, 1, 2) and the reactive force-field ReaxFF. Performances were evaluated by comparing several size-dependent features (such as relative stabilities, structural descriptors, and vibrational features) computed with the different methods. Various structures (ordered and amorphous) and sizes (from Pt_{13} to Pt_{561}) were considered in the datasets. ReaxFF molecular dynamics (MD) was employed to achieve the amorphization of cuboctahedral Pt_{147}, Pt_{309}, and Pt_{561} geometries, which were subsequently optimized with both the low-cost methods and the DFT reference, within a multilevel modeling approach. The structures were further annealed with GFN0-xTB MD. While DFTB performs quite well over all the selected structures, GFN2-xTB and the cheaper GFN0-xTB show a general predilection for amorphous geometries. The performances of GFN2-xTB are found to worsen with the increasing size of the system, while ReaxFF and GFN0-xTB undergo the opposite trend. We suggest that the semiempirical DFTB (and within certain limitations GFN0-xTB and ReaxFF) could be suited for fast screening through amorphous big-sized Pt NPs.

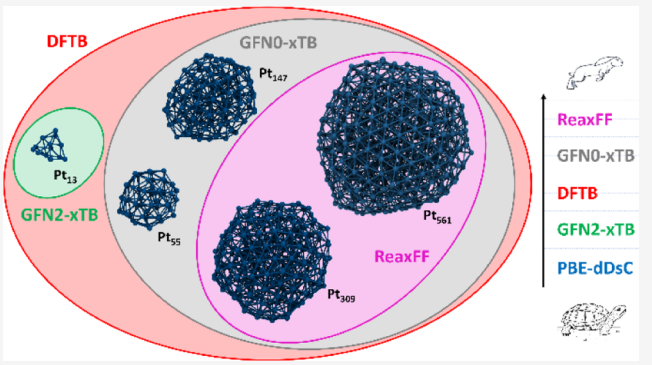

1. INTRODUCTION

The importance of metal nanoparticles (NPs) in modern technology has grown exponentially since scientists started studying their properties and engineering during the last century. Pt NPs display unique characteristics (resistance to oxidation, biocidal activity, plasmon resonance, etc.), which made them employable in a great variety of applications: from biosensors to electronics, catalysis, and more.[1,2] One of the most interesting features of Pt NPs is their ability to activate and sometimes dissociate many molecules of environmental and industrial relevance, such as H_2, CO, CO_2 and organic compounds.[3,4] The activity enhancement gained by dispersing metal nanoparticles of controlled size on support materials, such as oxides or carbons, has indeed given heterogeneous catalysts based on supported Pt NPs a central role in several catalytic processes,[5] like pollutant removal,[6,7] hydrogenation/dehydrogenation reactions,[8−11] naphtha reforming,[12,13] etc.

The fine understanding of the properties of Pt NPs is challenged by their complex and ductile structure, which is very sensitive to the chemical environment (reactants or nature of the support). Usually, Pt NPs display a great variety of sites whose coordination depends on the NP's shape, size, and structural disorder, giving birth to an overlap of contributions and convoluted experimental responses strongly depending on reaction conditions.[14] Hence, the atomic scale determination of these systems requires the use of cutting-edge characterization techniques in combination with state-of-the-art computational chemistry methods.[15−19] The advance of density functional theory (DFT) and the development of high-performance computing (HPC) facilities has led to numerous progresses in the understanding of the properties of Pt NPs through the last decades.[20] For instance, a great variety of shapes has been found for isolated Pt clusters,[21−24] while the interaction of Pt NP's with oxide supports[25−29] and various reactants (such as H_2 or CO) has been investigated for clusters ranging from 2 up to around 200 atoms.[28,30,31]

Nevertheless, one of the frontiers of the field arises from the fact that DFT can be employed for accurate calculations on simple systems featuring up to around a few hundred atoms,

Received: April 28, 2023
Revised: August 17, 2023
Published: September 7, 2023

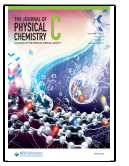

but it becomes rapidly too demanding when increasing the number of metallic atoms involved.[32,33] This aspect represents a strong limitation to the development of realistic models, often compelling researchers to rely on simplifications such as reduction of system's size and of nanostructure complexity.

The process of building reliable molecular models of metallic NPs comprehends a preliminary step in which many candidate structures have to be screened for a given NP size.[34] During this step, the potential energy surface (PES) has to be explored in order to find the most stable minima that can be relevant and populated at a given temperature.[35,36] Even though various algorithms, such as global optimization[24,37−39] and simulated annealing by *ab initio* molecular dynamics,[21,40−43] can be used to generate and explore candidate structures for metallic clusters, the main bottleneck of this step is the computational method employed to describe the PES. For example, an exhaustive PES exploration within a full-DFT approach can be carried out only for small and simple systems at a high computational cost. Adopting a multi-level modeling scheme often represents an efficient workaround, envisaging the exploitation of low-cost approximated methods (semiempirical (SE) functionals, force-fields (FF), neural network potentials, etc.) instead of DFT for the exploration of the PES.[23,44] Even though this strategy can massively reduce the computational cost of the process, the approximations on which these methods rely always entail an accuracy loss to some extent. Moreover, the stronger these approximations are, the weaker the transferability of the method. Thus, the accuracy of approximated low-cost methods must be thoroughly assessed against reference methods that are proven to be trustable for the systems at issue.

In this paper, we benchmark the performances of several low-cost computational methods for the computation of structural properties and size effects on Pt nanoparticles of stoichiometry Pt_{13}, Pt_{55}, Pt_{147}, Pt_{309}, and Pt_{561}. The semiempirical tested methods are density functional tight binding (DFTB)[45] and three methods belonging to the GFN extended tight binding family: GFN0-xTB,[46] GFN1-xTB,[47] and GFN2-xTB,[48] where the acronym "GFN" stands for "geometries, frequencies and noncovalent interactions". The ReaxFF[49,50] reactive force field was tested in the same fashion. DFTB and the ReaxFF are well-known methods that have already been frequently employed in heterogeneous catalysis.[51−58] On the other hand, the recently developed GFN methods were first benchmarked against high-level DFT, wave function theory (WFT), and experimental data mainly for organic and metal−organic compounds.[34,46−48] However, their promising applications reported in the past few years[59−62] together with their low computational cost and their atom-specific parametrization make their accuracy worth to be assessed on metal NPs as well.

Due to the lack of clear insight from the literature, our benchmark strategy for this study was built as follows. A small structural dataset containing 14 different Pt_{13} NPs, divided into amorphous and ordered structures, was considered to first test the performances of all the listed methods. The benchmark was performed by assessing their ability to reproduce relative stabilities, thermochemical parameters and structural descriptors (bond lengths, bond angles, and radii of gyration) computed at the PBE-dDsC[63,64] level for every NP of the dataset. An analogous approach is adopted for two sets of amorphous NPs of Pt_{13} (54 structures) and Pt_{55} (93 structures) stoichiometry, in order to evaluate the particle size effect. The ultimate task of the work will be to propose a cost-effective simulated annealing procedure combining ReaxFF and GFN0-xTB to generate reliable amorphous structures for large Pt_x NPs (x = 147, 309, 561). In the last section, this route is critically analyzed, pointing out its advantages and limits to overcome.

2. METHODOLOGY

2.1. Computational Details. DFT calculations were carried out within the plane-wave formalism, thanks to the VASP[65,66] code (version 5.4.4). The PBE exchange−correlation functional[63] was employed, setting an energy cutoff of 400 eV for Pt_{13} and Pt_{55} and 300 eV for Pt_{147}, Pt_{309}, and Pt_{561}. The choice of the PBE functional is due to its computational cost and general applicability,[67] allowing us to compute energies and geometries for the biggest NPs considered in this work, coupled with its relevance for simulating Pt and surfaces of transition metals in general.[68] The dDsC correction,[69] benchmarked for predicting molecular adsorption at Pt surfaces by Gautier et al.,[70] was added to take into account dispersion interactions, while core electrons were described with the PAW method.[71] To motivate our reference functional choice, we evaluated the performances of PBE, PBE-dDsC and PBEsol[72] on the *Pt_{13}small dataset* (details about the dataset are given in the next section). The comparison between relative energies computed with the three functionals is presented in Figure S1 of the Supporting Information. The small deviations (below 0.03 eV/atom) observed between the data obtained with the different functionals confirm that the impact of the reference GGA functional lies in the background if compared with the effect of a geometry optimization at the SE or FF level. A Gaussian smearing (σ = 0.05 eV) was applied to accelerate the convergence of the electronic iterations. The threshold for all the electronic energy minimizations was fixed to 10^{-7} eV. Spin-polarized calculations were performed for Pt_{13} and Pt_{55}. Geometries were optimized with the conjugate-gradient algorithm until the residual forces were below 0.005 eV/Å. Although geometry optimizations of NPs of sizes up to a few hundred of atoms are feasible at the PBE level, the same process is thousands of times faster if employing the low-cost methods at issue (Figure S2). Thus, understanding to what extent results obtained with the latter deviate from the PBE reference is crucial to safely exploit this massive gain in computational time.

DFTB calculations were carried out through the DFTB+ code (version 21.1).[45] Electronic energies were computed by setting a self-consistent charge (SCC) tolerance of 2.7×10^{-7} eV, a maximum angular momentum l_{max} = 2 and a Fermi−Dirac smearing featuring an electronic temperature of 500 K, following the settings chosen in ref 23. Geometries were optimized with the conjugate-gradient algorithm until the residual forces were below 5×10^{-4} eV/Å. The employed Slater−Koster parameters were adopted from ref 23.

Calculations performed with the GFNn-xTB methods were executed with the xTB code (version 6.4.0).[34] The threshold for convergence on electronic energies was set to 10^{-6} eV, while geometries were optimized through the ANCOPT algorithm with a convergence criterion of 0.01 eV/Å. We checked that using a tighter convergence criterion does not affect the results reported herein.

ReaxFF calculations were run within version 6.0 of the General Lattice Utility Program (GULP),[73] exploiting a parametrization derived in ref 74. The latter was made with the final aim of modeling the interaction between Pt clusters

https://doi.org/10.1021/acs.jpcc.3c02799
J. Phys. Chem. C 2023, 127, 18454−18465

and carbon platelets. The convergence criterion for geometry optimizations was set to 0.005 eV/Å.

All of the above-mentioned thresholds were chosen in order to avoid negative eigenvalues of the Hessian matrix during the computation of harmonic vibrational frequencies. To this purpose, the finite differences method was adopted for the VASP, DFTB+, and xTB code (elongation ±0.01 Å, $\pm 5 \times 10^{-5}$ Å, ±0.0025 Å, respectively), while analytical derivatives were computed with GULP. The computed vibrational frequencies were post-treated, through the laws of statistical thermodynamics,[75] to extract the vibrational contributions to the following thermodynamic quantities: enthalpy (H_{vib}), entropy (S_{vib}), and the Zero Point Vibrational Energy (ZPVE). The vibrational contribution to the Gibbs free energy (G_{vib}) at T = 300 K is computed as follows:

$$G_{vib} = H_{vib} - TS_{vib} + ZPVE \quad (1)$$

MD simulations were carried out in the *NVT* ensemble. ReaxFF MD was performed with the Nosé thermostat[76] and the velocity-Verlet algorithm at different temperatures (details are given in the next section). The employed time-step was 0.5 fs, while the total simulation time was 10 ps. The Berendsen thermostat[77] was employed for GFN0-xTB MD at 2000 K, with a time-step of 2 fs and a total simulation time of 50 ps.

2.2. Datasets and Models. The performances of the chosen low-cost methods were evaluated by investigating four structural datasets (coordinates in XYZ format of PBE-dDsC structures for each data set are given in the Supporting Information):

- *Pt_{13}small dataset*: 14 structures divided into ordered and amorphous

  Coordinates of structures belonging to this dataset have different origins: the structures cbpt (capped biplanar triangle), nbp (new biplanar), scsc (side-capped simple cubic), dscsc (disordered side-capped simple cubic), tcsc (top-capped simple cubic), bbp (buckled biplanar), and ico (icosahedral) are taken from ref 21. The structures sa and sa2 are still taken from ref 21 and differ from the previous ones as they are generated through first-principles simulated annealing (hence the "sa" terminology). The structures go2, go3, and go4 are taken from ref 23 (where "go" stands for "global optimization"). The structures nsx0 and nsx2 were obtained by optimizing at GFN0-xTB and GFN2-xTB level amorphous structures from previous DFT calculations.
- *Pt_{13}amorphous dataset*: 54 amorphous structures (coordinates adopted from ref 23)
- *Pt_{55}amorphous dataset*: 93 amorphous structures (coordinates adopted from ref 23)
- *Multi-sized dataset*: 5 amorphous structures of stoichiometry Pt_{13}, Pt_{55}, Pt_{147}, Pt_{309}, Pt_{561} (presented in Figure 1) considered to evaluate the size-dependency of the performances of the tested methods.

  Pt_{13} and Pt_{55} structures in this dataset correspond to the lowest-energy structures of the *Pt_{13}* and *Pt_{55}amorphous datasets*, respectively. Amorphous Pt_{147}, Pt_{309}, and Pt_{561} were obtained through the amorphization of the ordered cuboctahedral geometry, as schematized in Figure 2A. Cuboctahedral nanoparticles were first cut out of the Pt bulk and subsequently subjected to ReaxFF MD. Different temperatures, ranging from 800 to 2700 K, were tested to find the minimal temperature to shake cuboctahedral geometries in order to explore various conformational states. A complete amorphization of the structure was achieved at 2000 K for Pt_{147}, 2500 K for Pt_{309}, and 2700 K for Pt_{561}. The lowest-energy structure of each MD run was quenched at 0 K with ReaxFF, obtaining an amorphous ReaxFF geometry for each stoichiometry. The geometries of the obtained structures were optimized with the low-cost methods, as well as with PBE-dDsC. GFN0-xTB geometries were finally annealed through GFN0-xTB MD, aiming to enhance the accuracy of the generated NP models through higher-level MD. Several candidate low-lying energy conformations per stoichiometry were quenched at 0 K with GFN0-xTB in this case, taking as output only the lowest-energy structure resulting after PBE-dDsC single point energy evaluations. Notably, for this part of the study, we will only compare energies evaluated at our reference level of theory (PBE-dDsC), as will be discussed in section 3.3. The energies computed at the GFN0-xTB level are not considered. The sampling approaches for ReaxFF and GFN0-xTB MD are exemplified in Figure 2B for Pt_{147}.

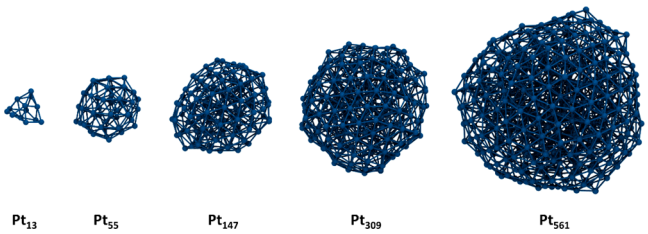

Figure 1. Examples of structures of NPs belonging to the multi-sized dataset optimized at the PBE-dDsC level at 0 K.

Structures belonging to the *Pt_{13}small dataset* were first optimized at the PBE-dDsC level. The thus obtained geometries were further optimized with all the low-cost methods, and we evaluated their performances by comparing bond lengths, bond angles, radii of gyration, relative stabilities, and thermochemical parameters computed by the low-cost methods with the reference PBE-dDsC (section 3.1). The benchmark on the *Pt_{13}amorphous dataset* and *Pt_{55}amorphous dataset* (section 3.2) was carried out analogously, although vibrational frequencies (and thus thermochemical parameters) were not computed. Moreover, GFN1-xTB was not tested on the *Pt_{13}* and *Pt_{55}amorphous datasets* due to the poor performances exhibited for the *Pt_{13}small dataset*. As outlined in Figure 2A, all the structures of the *multi-sized dataset* (section 3.3) were subjected to a PBE-dDsC single point energy evaluation. Thus, the outcome of the employed multi-level procedure was inspected by analyzing the deviations on PBE-dDsC electronic energies and bond lengths between the low-cost and PBE-dDsC geometries. GFN1-xTB was not employed in this section for the aforementioned reason, while GFN2-xTB was discarded because of the inability to reach a convergence in SCC calculations for Pt_{147}, Pt_{309}, and Pt_{561}. This work is mainly focused on amorphous NPs since Pt NPs are experimentally known to show a general preference for amorphous morphologies which vanishes when increasing the particle size.[78] Notably, after some preliminary tests, we testified the inability of

https://doi.org/10.1021/acs.jpcc.3c02799
J. Phys. Chem. C 2023, 127, 18454−18465

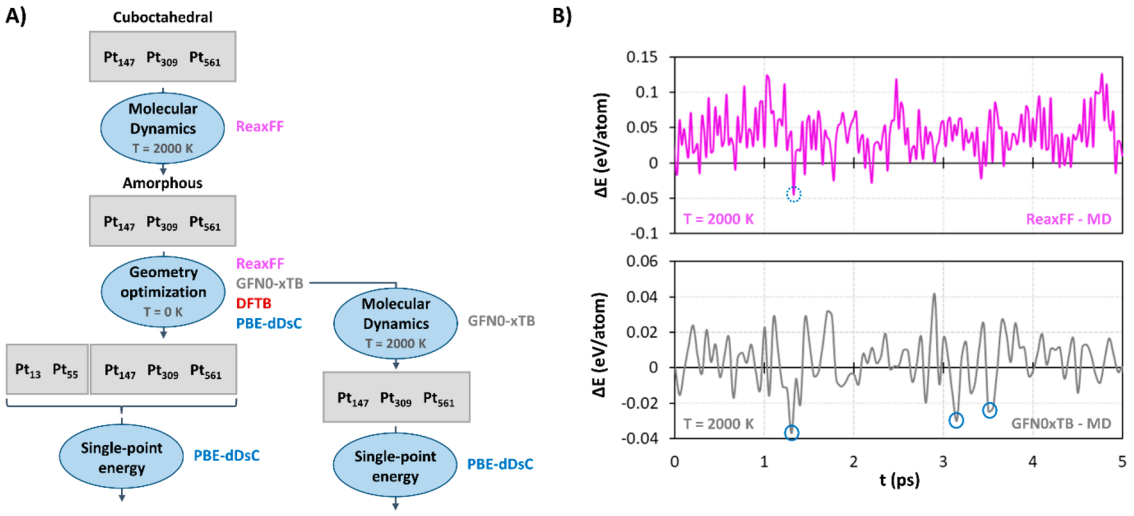

Figure 2. (A) Flowchart of the multi-level procedure adopted to build Pt_{147}, Pt_{309}, and Pt_{561} NPs within the *multi-sized dataset*. (B) Energy (referred to the starting point) evolution versus simulation time for 5 ps of ReaxFF (pink) and GFN0-xTB (gray) MD for Pt_{147}. The lowest ReaxFF structure (dashed circle) was quenched at 0 K with ReaxFF. Among the highlighted lowest-energy GFN0-xTB structures (solid circles), only the most stable conformer according to PBE-dDsC energies was chosen as the output of the procedure.

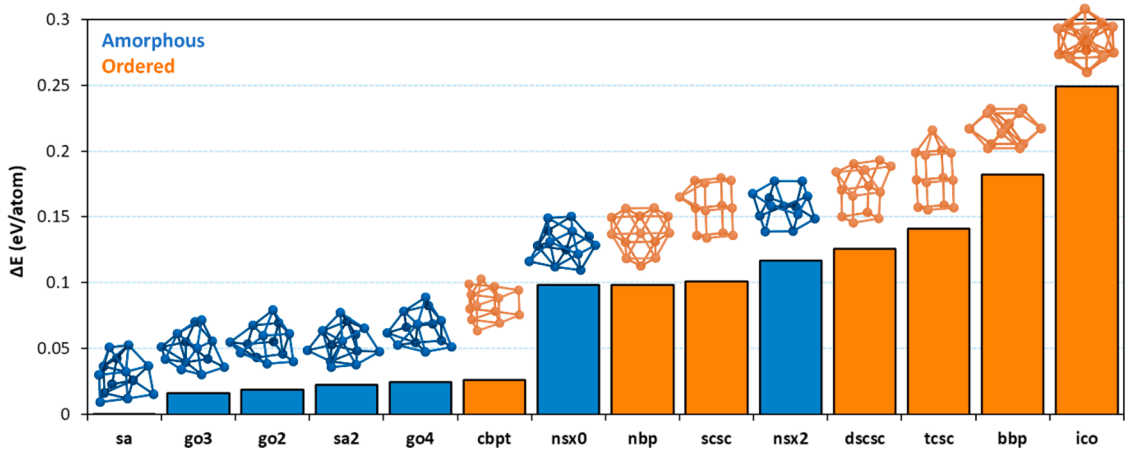

Figure 3. Relative stability (with respect to the global minimum) of all the structures of the Pt_{13} small dataset, ranked according to their electronic energy computed at PBE-dDsC level. Amorphous structures are represented in blue, while ordered ones are in orange.

the GFN methods to retain cuboctahedral geometries for Pt_x NPs with $x > 13$.

The graphical visualization and structural manipulation of the NPs was performed with VESTA (version 4.0.0).[79] Images of molecular models were rendered with VMD.[80] The kernel density estimate (KDE) plots presented in section 3.2 were created with the Python library Seaborn.[81]

3. RESULTS AND DISCUSSION

3.1. Pt_{13} Small Dataset. All of the structures optimized at the PBE-dDsC level are ranked according to their electronic energy in Figure 3. As outlined in section 2, the 14 Pt_{13} NPs are divided into two classes: "amorphous" and "ordered". While among the structures of the "amorphous" class, the atoms are "randomly" organized in space, the atomic positions in the "ordered" structures are subjected to stricter geometrical constraints. The dispersion-corrected GGA electronic energies suggest that for the Pt_{13} system ordered structures are generally less stable than the amorphous ones. This trend is consistent with the fact that the arrangement of atoms in ordered structures is either cut out of the bulk or built to fit specific geometric shapes. On the other hand, most of the amorphous structures (with the exception of sa, the most stable structure, found by simulated annealing)[21] shown here were obtained through a global optimization procedure[23] that was explicitly devoted to find the most stable geometries for this system.

One notable result about this dataset concerns the cuboctahedral geometry, which has been widely employed as a model nanoparticle for many metals due its straightforward extraction from an fcc crystalline lattice.[22,82] According to the analysis of vibrational frequencies, the optimized cuboctahedral structure (ΔE = 0.24 eV/atom with respect to the sa global minimum) displays residual imaginary frequencies corresponding to compression along the axis normal to the squared facets. A line minimization was performed to scan the normal coordinate associated with the imaginary frequency in order to find the minimum conformation. After the line-minimization procedure, the reoptimized geometry collapsed to the bbp structure, implying the removal of the cuboctahedral Pt_{13} from our dataset. This cuboctahedral structure was kept in ref 21 without confirming by frequency analysis if it was a true

https://doi.org/10.1021/acs.jpcc.3c02799
J. Phys. Chem. C 2023, 127, 18454−18465

minimum. Nevertheless, the overall energy trend is consistent with the one reported for sa, nbp, bbp, ico, and cub in ref 21.

After reoptimizing PBE-dDsC structures with the low-cost methods, a detailed analysis of their performances was achieved by extracting and comparing different features of the NPs: geometries, relative stabilities, and thermochemical parameters.

3.1.1. Geometries. To represent the geometrical features of each NP, we extracted the Pt−Pt distances between nearest neighbors (Figure 4A), the angles between three nearest neighbors Pt atoms (Figure 4B) and the radius of gyration (R_g, Figure 4C). The errors of the tested low-cost methods for each nanoparticle with respect to the PBE-dDsC reference are reported in Figure 4. Only the errors for the three best performing methods are shown in the main text due to the poor results obtained with ReaxFF and GFN1-xTB. Histograms for all the methods are given in Figure S3.

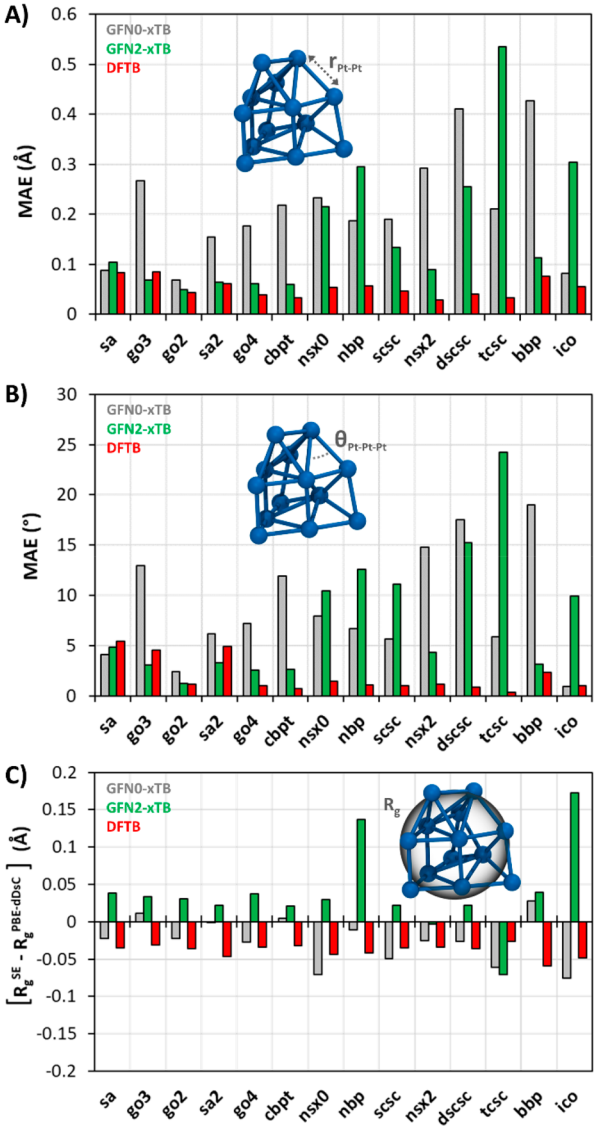

Figure 4. Mean Absolute Error (MAE) for bond lengths (A) and bond angles (B) and the signed deviation from PBE-dDsC for the gyration radius R_g (C) made by semiempirical methods (SE): GFN0-xTB (gray), GFN2-xTB (green), and DFTB (red).

The averaged mean absolute errors (MAEs) computed separately for amorphous and ordered structures are reported in Table 1. As emerges both from the histograms in Figure 4 and from Table 1, DFTB outperforms GFN0-xTB and GFN2-xTB in most cases, showing errors below 0.1 Å for bond lengths and generally below 5° for bond angles. GFN2-xTB systematically shows lower errors on amorphous geometries (competing with DFTB), while its performances become poor when evaluated on ordered structures. The results obtained with GFN0 are not undergoing any specific trend. However, it is worth noting that for R_g, GFN0-xTB exhibits the lowest deviation (in absolute value) for both amorphous and ordered structures. Our interpretation of this behavior is that, even though the "local" geometry is not strictly retained from DFT, the global information on the shape of the particle is not completely lost.

3.1.2. Relative Stabilities. In this section, we aim to assess the performances of our low-cost methods on the energetic ranking of the structures belonging to the *Pt_{13}small dataset*. The energies are expressed here as relative stabilities with respect to the global minimum, as was done for Figure 3. For each geometry optimized at the PBE-dDsC level, we compare the PBE-dDsC energy with the energy obtained with the chosen low-cost method on the same atomic conformation, thus neglecting the effect of SE geometry optimization in the first place. We express the raw results in the form of histograms (Figure 5, full columns), while we quantify the degree of agreement between the DFT and SE energies by means of a linear regression analysis, which is performed separately for amorphous and ordered structures. The regression parameters (slope and determination coefficient (R^2)) are compactly given in Table 2, while the relative scatter plots are presented in panels A, C and E of Figure S4.

Relying on the reported values of R^2, the regression analysis shows itself to be rather inglorious for GFN0-xTB energies, classifying again DFTB as the best performing method (in line with the parametrization of ref 23), followed by GFN2-xTB. Here, the different behavior for ordered and amorphous structures is evident not only for GFN2-xTB but also for GFN0-xTB and DFTB, even though for the latter the difference is almost negligible. Despite the poor results of GFN0-xTB, the performances of GFN2-xTB are strongly morphology-dependent, being competitive with those of DFTB only for the amorphous structures. The generally coarse results of GFN0-xTB are reflected in the histograms of Figure 5B, from which it appears its inability to reproduce the stability trend depicted by PBE-dDsC energies (Figure 5A). While both GFN2-xTB and DFTB perform well for amorphous structures, they behave differently for the ordered ones: DFTB is slightly underestimating their stability (Figure 5D), while the trend is less uniform for GFN2-xTB (Figure 5C).

At this point, we mean to take into account the effect of geometry optimization at the SE level. To this purpose, we carried out an analogous analysis by comparing the PBE-dDsC relative energy with the relative energy obtained with the chosen low-cost method on the same NPs after geometry optimization. The corresponding histograms are presented in Figure 5 (striped columns), while the regression parameters are reported in brackets in Table 2 (the relative scatter plots are presented in Figure S5).

The value of R^2 generally decreases upon geometry optimization with SE methods, which is consistent with the

https://doi.org/10.1021/acs.jpcc.3c02799
J. Phys. Chem. C 2023, 127, 18454−18465

Table 1. Averaged Errors on Bonds, Angles and R_g for the Small Pt_{13} Dataset

	bonds MMAE (Å)[a]			angles MMAE (deg)[a]			R_g MAE (Å)[b]		
	GFN0-xTB	GFN2-xTB	DFTB	GFN0-xTB	GFN2-xTB	DFTB	GFN0-xTB	GFN2-xTB	DFTB
Amorphous	0.18	0.09	0.06	7.9	4.2	2.8	0.026	0.028	0.037
Ordered	0.26	0.24	0.05	10.9	10.3	1.1	0.033	0.066	0.040

[a]The averaged error on bond lengths and angles is expressed as Mean MAE (MMAE). [b]The average error on R_g is expressed as a MAE. All the quantities are computed separately on amorphous and ordered structures to highlight the morphology-dependent behavior of the tested methods.

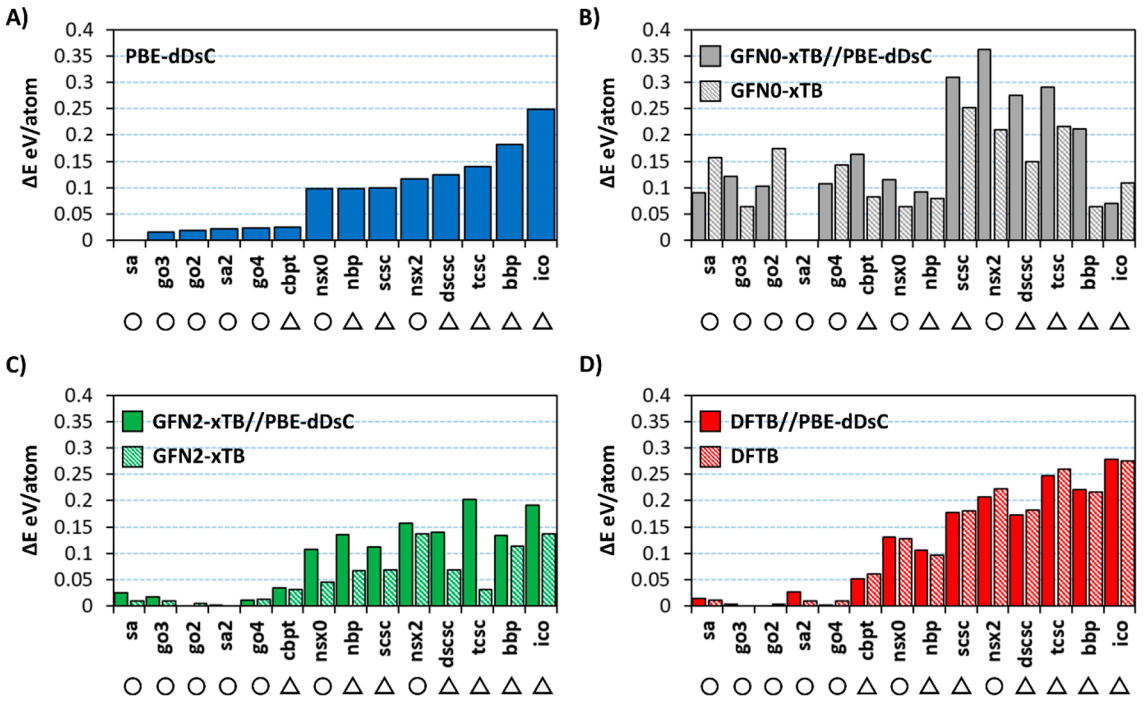

Figure 5. Relative stabilities (with respect to the global minimum) of the structures of the Pt_{13} small dataset, computed with PBE-dDsC (A), GFN0-xTB (B), GFN2-xTB (C), and DFTB (D). Full columns correspond to single point energy evaluations performed on the frozen PBE-dDsC geometry, while striped columns report the SE energy of the same NP after geometry optimization. Circles indicate amorphous structures, while triangles indicate ordered ones.

Table 2. Determination Coefficients and Slopes of the Regression Analysis Performed on Relative Stabilities (PBE-dDsC versus SE Energy)

	GFN0-xTB//PBE-dDsC[a] (GFN0-xTB)[b]		GFN2-xTB//PBE-dDsC[a] (GFN2-xTB)[b]		DFTB//PBE-dDsC[a] (DFTB)[b]	
	R^2	Slope	R^2	Slope	R^2	Slope
Amorphous	0.53 (0.004)	0.30 (0.13)	0.90 (0.77)	0.70 (0.82)	0.93 (0.93)	0.54 (0.50)
Ordered	0.06 (0.005)	−0.18 (−0.06)	0.63 (0.70)	1.00 (1.50)	0.82 (0.75)	0.80 (0.77)

[a]The regression was performed on relative stabilities computed by SE methods on frozen PBE-dDsC geometries. [b]The regression was performed on relative stabilities computed after reoptimization at SE level.

natural action of forces that modify atomic coordinates during geometry optimizations. The case of GFN2-xTB on ordered structures is less trivial. Even though the higher value of R^2 suggests a better correlation between data points, the high slope value (Table 2) indicates a general compression of the energetic range covered by PBE-dDsC, which is reflected in the histograms (Figure 5C). Moreover, the significant difference between the relative stabilities of ordered structures before and after GFN2-xTB geometry optimization is consistent with the significant MAE on bond lengths and angles discussed in section 3.1.1. DFTB is less sensitive to geometry optimization than the other methods for all structures and provides a more coherent stability trend with respect to PBE-dDsC.

3.1.3. Vibrational Frequencies and Thermochemical Parameters. While the previous section checked how the semiempirical methods are able to identify the energy minima of the potential energy surface, we now aim to analyze how these methods describe the fluctuation of the systems in the close vicinity of those energy minima. First, harmonic vibrational frequencies were computed for each structure at different levels of theory. Information about the deviations of the unprocessed vibrational frequencies computed with low-cost methods with respect to PBE-dDsC can be found in Figure S6.

According to the mean bias errors (MBE) presented in Table 3 and the histograms of Figure 6 and Figure S7, deviations on the vibrational enthalpy (H_{vib}) plus ZPVE are found to be negligible compared with the entropic term.

https://doi.org/10.1021/acs.jpcc.3c02799
J. Phys. Chem. C 2023, 127, 18454−18465

Table 3. Averaged Errors on G_{vib}, $-TS_{vib}$, H_{vib}, and ZPVE for the Small Pt_{13} Dataset

	MBE [G_{vib}] (kJ/mol)	MBE [$-TS_{vib}$] (kJ/mol)	MBE [H_{vib}] (kJ/mol)	MBE [ZPVE] (kJ/mol)
GFN0-xTB	8.0	6.9	−1.3	2.4
GFN2-xTB	−16.2	−16.2	2.8	−2.7
DFTB	12.7	11.3	−2.4	3.8

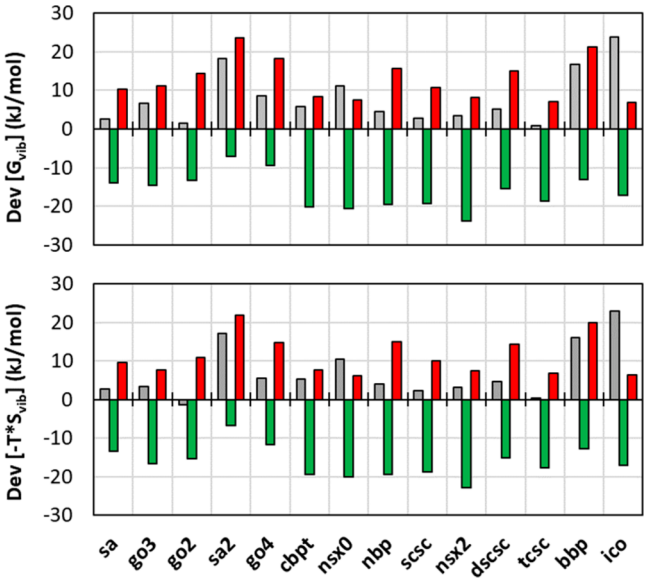

Figure 6. Deviations of GFN0-xTB (gray), GFN2-xTB (green), and DFTB (red) with respect to PBE-dDsC on the computation on the vibrational free energy and entropy (TS_{vib}) at T = 300 K. We did not plot Dev [Hvib + ZPVE] since it was fully balanced around 0 and always below 4 kJ/mol.

Hence, since the vibrational free energy is computed as reported in eq 1, the error on G_{vib} comes predominantly from the $-TS_{vib}$ term. The main contribution to H_{vib} comes from high-frequency modes,[83] which are most likely associated with close bonding and stretching modes. S_{vib}, on the other hand, is more sensitive to low-frequency modes, corresponding to concerted movements of the whole NP. Thus, the negligible error on H_{vib} signifies that all the methods are well describing the shape of the potential well associated with high-frequency modes and thus to close bonding, where it is less true for the concerted vibrations. Nevertheless, the magnitude of G_{vib} remains rather small (less than 16 kJ/mol), which implies that the relative stability of all structures is not modified at T = 300 K by vibrational contributions whatever the method used (Figure S8).

Analyzing the histograms in Figure 6, two main observations can be made: GFN0-xTB shows the smallest deviation from the standard PBE-dDsC and the deviation of GFN2-xTB follows the opposite trend with respect to the other two methods. This behavior indicates that for low-frequency modes, while DFTB and GFN0-xTB are computing tighter potential wells with respect to PBE-dDsC, the same potential wells computed by GFN2-xTB are looser. This means that GFN2-xTB, in contrast to DFTB and GFN0-xTB, underestimates force constants for vibrations in which the whole nanoparticle is involved.

3.2. Pt_{13} and Pt_{55} Amorphous Datasets. As described in section 2.2, a procedure analogous to the one applied to the *Pt_{13}small dataset* was adopted for the two large datasets of amorphous Pt_{13} and Pt_{55} NPs. All the geometries optimized at PBE-dDsC level were reoptimized with GFN0-xTB, GFN2-xTB, DFTB, and ReaxFF. The agreement of the tested methods with the PBE-dDsC reference was evaluated by comparing three geometric descriptors (bond lengths, bond angles, and R_g) and the relative energies of the structures belonging to the two datasets.

Figure 7 reports the distribution of the signed deviation on bond lengths, bond angles, and R_g computed for all the tested low-cost methods, for both the Pt_{13} and Pt_{55} amorphous datasets. Since the signed deviation is a discrete variable in these cases, continuous probability density functions were estimated through the Kernel Density Estimation (KDE) procedure, with the Seaborn library[81] available in the Python code. The KDE plots for each geometric descriptor are computed by employing the same smoothing factor, thus legitimating the comparison between the probability density functions of the two datasets. Additional information about the computation of KDE plots can be found in section S7 of the Supporting Information.

The differences in the distributions between Pt_{13} and Pt_{55} reveal that the performances of DFTB and GFN0-xTB are generally improving while increasing the particle size: the distributions are getting narrower and shifted toward zero. GFN2-xTB seems to undergo the opposite trend; indeed, the distributions of the deviation for bonds and angles are widening when moving from Pt_{13} to Pt_{55}, while the behavior of the deviation on R_g is less clear. The performances of ReaxFF are generally poor and show only a slight improvement for Pt_{55} with respect to Pt_{13}. DFTB proves to be the best method, although it causes a small and systematic compression of bond lengths, which is also reflected in the deviation on R_g. GFN0-xTB is showing the biggest improvements, becoming competitive with DFTB and outperforming it for R_g.

The plots reported in Figure S4B, S4D, and S4F are conceived to inspect the correlation between relative energies computed at PBE-dDsC level with relative energies computed with the tested low-cost methods for the structures belonging to the Pt_{13} amorphous dataset. In this case, data show that the energy range in which the amorphous isomers of Pt_{13} lie is far smaller than the accuracy of a GGA functional such as PBE. As illustrated in Figure S9, the data regarding amorphous Pt_{55} NPs exhibit also a very narrow energy fluctuation. Hence, it is beyond the accuracy level to discuss any correlation between electronic relative energies for these sets of amorphous NPs.

3.3. Towards Big-Sized Nanoparticles. Amorphous geometries for nanoparticles of stoichiometry Pt_{147}, Pt_{309}, and Pt_{561} were obtained through the procedure described in section 2.2. As a preliminary remark, the relative energies (calculated at PBE-dDsC level) between amorphous and cuboctahedron clusters show that for clusters smaller than 309 atoms, amorphous clusters are more stable than the cuboctahedral isomers (Figure S10). For a cluster size of 561 atoms, the cuboctahedron becomes more stable. Interestingly, this trend is found in qualitative agreement with the experimental observation showing the predominance of amorphous clusters for sizes smaller than ∼250 atoms.[78] Nevertheless, to overcome the limitation of considering only cuboctahedral isomers, such a result should prompt a more systematic theoretical investigation comparing the energies of amorphous clusters found in the present studies with ordered clusters exhibiting much more diverse morphologies (other than

https://doi.org/10.1021/acs.jpcc.3c02799
J. Phys. Chem. C 2023, 127, 18454−18465

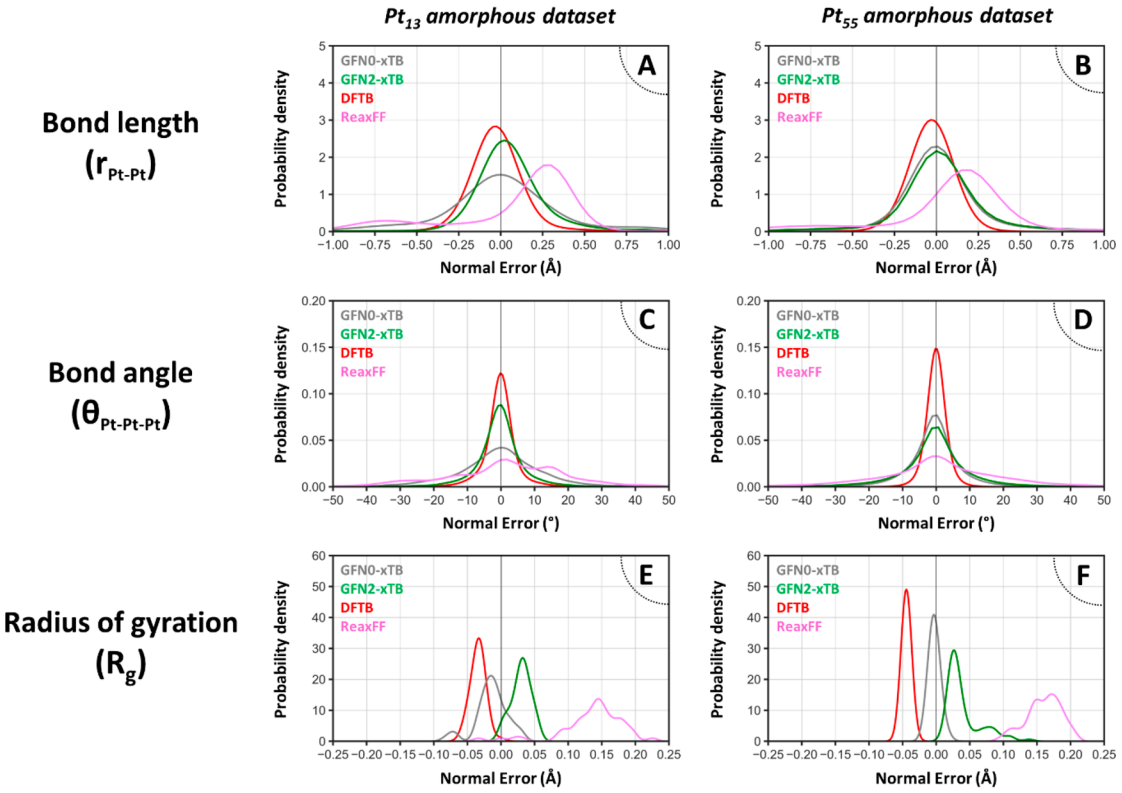

Figure 7. Distribution of the signed deviation on bond lengths (A, B), bond angles (C, D), and radii of gyrations (E, F) for DFTB (red), GFN2-xTB (green), GFN0-xTB (gray), and ReaxFF (pink) with respect to PBE-dDsC values for the Pt_{13} and Pt_{55} amorphous datasets.

cuboctahedral ones). Concerning only the amorphous nanoparticles, we inspected the agreement of the tested low-cost methods with the DFT standard (as well as the performances of xTB MD) by plotting, for each nanoparticle, the deviation between its pure PBE-dDsC energy and its PBE-dDsC energy evaluated as single point on SE or FF geometry. The energy deviation (ΔE) reported in Figure 8A is computed as follows:

$$\Delta E = E_{\text{PBE-dDsC // Low-cost}} - E_{\text{PBE-dDsC}} \quad (2)$$

Given the strong dependency of the electronic energy on the atomic coordinates, the quantity "ΔE" defined in eq 2 is exploited here, together with the mean Pt−Pt distance, to weigh the discrepancy between the benchmark PBE-dDsC structures and the low-cost ones (Figure 8).

The systematic decrease in the deviation (ΔE) of ReaxFF coupled with the increase in the system's size can be at least partially linked to its parametrization, which has been carried out initially on Pt_{100} clusters.[74] However, the energy deviation remains quite large to be exploitable (around 0.16 eV/atom for Pt_{561}). Moreover, ReaxFF completely reverses the canonic relationship between the intermetallic distances and the NP's size. GFN0-xTB follows the opposite trend and shows a significantly higher deviation for Pt_{147}, Pt_{309}, and Pt_{561} than for Pt_{13} and Pt_{55}. Although this energy deviation is rather comparable with the one observed for ReaxFF, the mean Pt−Pt distance on GFN0-xTB structures shows good agreement with PBE-dDsC compared with structures optimized with the other low-cost methods. In order to attempt to decrease the ΔE for GFN0-xTB and in light of the rather low computational cost of GFN0-xTB MD, the GFN0-xTB geometries of Pt_{147}, Pt_{309}, and Pt_{561} were further annealed during 50 ps, as explained in section 2.2. This additional

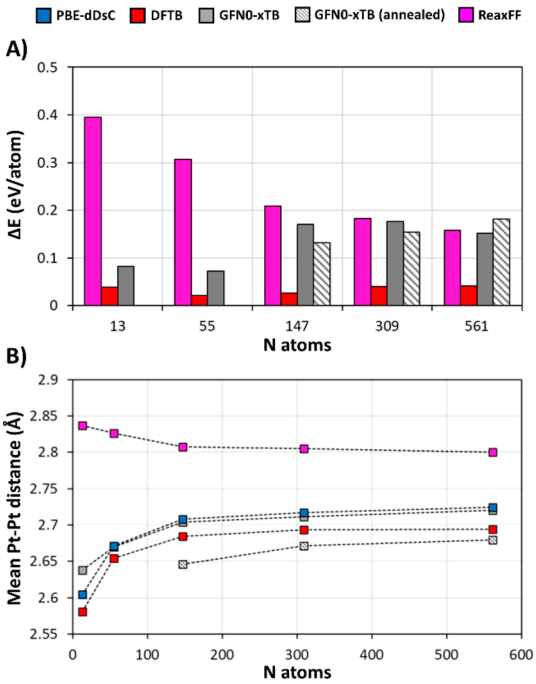

Figure 8. (A) Electronic energy difference between the full PBE-dDsC energy and the PBE-dDsC energy evaluated on DFTB (red), GFN0-xTB (gray), or ReaxFF (pink) geometry. The gray stripes represent the difference between the full PBE-dDsC energy and the PBE-dDsC energy evaluated on a geometry annealed with GFN0-xTB molecular dynamics. (B) Evolution of the mean Pt−Pt distance with particle size for PBE-dDsC (blue), DFTB (red), GFN0-xTB (gray), annealed GFN0-xTB (striped gray), and ReaxFF (pink) geometries.

https://doi.org/10.1021/acs.jpcc.3c02799
J. Phys. Chem. C 2023, 127, 18454−18465

annealing step succeeded in modestly reducing the ΔE of GFN0-xTB structures for Pt_{147} and Pt_{309} by about 0.03 eV and did not reduce the energy deviation for Pt_{561}. In this latter case, longer MD simulation times are probably required. Even though geometries obtained from GFN0-xTB molecular dynamics do not provide significant improvements in ΔE (eq 2, all computed at the PBE-dDsC level) with respect to geometries obtained thanks to ReaxFF for the largest particles, GFN0-xTB molecular dynamics is still able to provide reliable results for Pt−Pt bond lengths. Unfortunately, the averaged Pt−Pt bond length of annealed GFN0-xTB structures is not straightforwardly comparable with the others since they are generated through a completely different approach. Finally, DFTB proves itself as the best-performing low-cost method, even though it causes a systematic compression of Pt NPs (Figure 8B). Its low energy deviation (less than 0.05 eV/atom) reported for all of the investigated particle sizes states that the good performances exhibited by DFTB for Pt_{13} and Pt_{55} are maintained when increasing the number of atoms up to a few hundred. Since the employed parametrization for DFTB has been carried out solely on Pt_{13} and Pt_{55} clusters,[23] this indicates a good transferability of the set of parameters.

4. CONCLUSIONS

In this work, we assessed the performances of low-cost computational methods for the prediction of structural features and energetics of Pt nanoparticles of stoichiometry Pt_{13}, Pt_{55}, Pt_{147}, Pt_{309}, and Pt_{561}. The chosen low-cost methods were the semiempirical DFTB, GFN0-xTB, GFN1-xTB, GFN2-xTB, and ReaxFF, while the reference DFT functional was the dispersion-corrected PBE-dDsC. We carried out the benchmark study on four structural datasets, composed of (1) 14 amorphous and ordered Pt_{13} NPs, (2) 54 amorphous Pt_{13} NPs, (3) 93 amorphous Pt_{55} NPs, and (4) 5 amorphous NPs of stoichiometry Pt_x (x = 13, 55, 147, 309, 561). In the light of the discussed data, the following conclusions can be drawn.

DFTB is by far the method showing the best performances. Its parametrization, carried out on Pt_{13} and Pt_{55} NPs, grants good reproduction of properties for NPs of the same size. The good agreement with the DFT standard shown for NPs of bigger sizes also proves the good transferability of the parametrization. The performances of the remaining methods are found to be morphology- and size-dependent. GFN2-xTB produces reasonable results for amorphous Pt_{13} clusters, though not for ordered ones. Moreover, its performances worsen when increasing the cluster's size from 13 to 55, before failing the electronic SCC when further increasing the size of the system. While the agreement between GFN0-xTB and the DFT standard is quite poor for Pt_{13}, the method provides a satisfactory prediction of structural features for amorphous Pt_{55} geometries, making it competitive with DFTB. GFN0-xTB is slightly worsening for Pt_{147}, Pt_{309}, and Pt_{561} with respect to smaller clusters, though it outperforms the other methods on the averaged Pt−Pt bond length. ReaxFF behaves in the opposite way. Starting from considerably poor performances for Pt_{13} and Pt_{55} (both for geometries and for energies), its results get better for bigger NPs, becoming competitive with GFN0-xTB for Pt_{561}, even though the average Pt−Pt bond length is still not well represented. One last notable conclusion can be drawn about vibrational frequencies: independently from the parametrization and level of theory, all of the tested methods show a deviation in the description of vibrational features of Pt_{13}. Since the largest part of the error lies on the vibrational entropy, this indicates a shared intrinsic difficulty in the description of potential wells related to collective vibrations. However, the error on G_{vib} is around 10 kJ/mol for DFTB, and even smaller for GFN0-xTB. Although this is far from being perfect, it still represents a good compromise due to the gain in CPU.

Considering what is here summarized, DFTB turns out to be the most cost-effective method for predicting geometries and energetics of Pt NPs of all of the investigated sizes and morphologies. However, since our task is to propose a low-level computational method for fast screening through candidate structures within the "multilevel modelling" of phenomena involving Pt NPs, a few final remarks have to be made. Although DFTB is the best performing method presented in this paper, the cheaper GFN0-xTB and ReaxFF should not be entirely discarded. The systematic error on structural parameters shown by ReaxFF suggests that a reoptimization of the parametrization could sensibly improve its performances. At the same time, the atom-specific parametrization on which GFN0-xTB relies indeed allows one to effortlessly include other atoms into the simulation (while DFTB would require a reparametrization), thus opening the path to the simulations of structures involving adsorbates or nanoalloys.

■ ASSOCIATED CONTENT

Supporting Information

The Supporting Information is available free of charge at https://pubs.acs.org/doi/10.1021/acs.jpcc.3c02799.

Comparison between different GGA functionals on the details on the Pt_{13} small dataset (S1), CPU times (S2), additional data concerning histograms reporting errors on geometries (S3), regression analysis on relative stabilities (S4), thermochemical properties (S5) and relative stabilities (S6) for the Pt_{13} small dataset, theoretical background and additional data concerning KDE plots (S7), additional data concerning the regression analysis on relative stabilities for the Pt_{13} and Pt_{55} amorphous dataset (S8); amorphization energies (S9) (PDF)

Coordinates optimized at PBE-dDsC level in XYZ format of (1) all the structures of the Pt_{13} small dataset, (2) the five lowest-energy structures of the Pt_{13} amorphous dataset, (3) the five lowest-energy structures of the Pt_{55} amorphous dataset, and (4) the amorphous Pt_{147}, Pt_{309}, Pt_{561} (TXT)

■ AUTHOR INFORMATION

Corresponding Authors

Alberto Ricchebuono − *Department of Chemistry, INSTM and NIS Centre, University of Torino, Torino I-10135, Italy;* orcid.org/0000-0003-0497-3785; Email: alberto.ricchebuono@unito.it

Céline Chizallet − *IFP Energies nouvelles, 63960 Solaize, France;* orcid.org/0000-0001-5140-8397; Email: celine.chizallet@ifpen.fr

Authors

Eleonora Vottero − *Department of Chemistry, INSTM and NIS Centre, University of Torino, Torino I-10135, Italy;* orcid.org/0000-0002-0183-0669

Andrea Piovano − *Institut Laue-Langevin (ILL), Grenoble 38000, France;* orcid.org/0000-0002-5005-6307
Elena Groppo − *Department of Chemistry, INSTM and NIS Centre, University of Torino, Torino I-10135, Italy;* orcid.org/0000-0003-4153-5709
Pascal Raybaud − *IFP Energies nouvelles, 63960 Solaize, France;* orcid.org/0000-0003-4506-5062

Complete contact information is available at: https://pubs.acs.org/10.1021/acs.jpcc.3c02799

Notes

The authors declare no competing financial interest.

■ ACKNOWLEDGMENTS

This work was performed using HPC resources from the supercomputers ENER440 of IFPEN, Fram of the Norwegian academic HPC infrastructure (for which we thank Prof. Stian Svelle and Prof. Silvia Bordiga), and OCCAM of the University of Torino. We thank Dr. Maxime Van Den Bossche for the sharing of molecular models of amorphous Pt_{13} and Pt_{55} clusters, fully described in ref 23. We thank Prof. Tomáš Bučko (Comenous University Bratislava) for providing us with the python scripts used for post-treating vibrational frequencies and for line-minimization procedures.

■ REFERENCES

(1) Xu, Y.; Zhang, B. Recent Advances in Porous Pt-Based Nanostructures: Synthesis and Electrochemical Applications. *Chem. Soc. Rev.* **2014**, *43* (8), 2439−2450.
(2) Khan, M. A. R.; Mamun, M. S. Al; Ara, M. H. Review on Platinum Nanoparticles: Synthesis, Characterization, and Applications. *Microchem. J.* **2021**, *171* (September), No. 106840.
(3) Chen, A.; Holt-hindle, P. Platinum-Based Nanostructured Materials: Synthesis, Properties, and Applications. *Chem. Rev.* **2010**, *110*, 3767−3804.
(4) Campelo, J. M.; Luna, D.; Luque, R.; Marinas, J. M.; Romero, A. A. Sustainable Preparation of Supported Metal Nanoparticles and Their Applications in Catalysis. *ChemSusChem* **2009**, *2* (1), 18−45.
(5) Boudart, M. Catalysis by Supported Metals. *Adv. Catal.* **1969**, *20* (C), 153−166.
(6) Heck, R. M.; Farrauto, R. J. Automobile Exhaust Catalysts. *Appl. Catal. A Gen.* **2001**, *221* (1), 443−457.
(7) Gänzler, A. M.; Casapu, M.; Vernoux, P.; Loridant, S.; Cadete Santos Aires, F. J.; Epicier, T.; Betz, B.; Hoyer, R.; Grunwaldt, J. D. Tuning the Structure of Platinum Particles on Ceria In Situ for Enhancing the Catalytic Performance of Exhaust Gas Catalysts. *Angew. Chem., Int. Ed.* **2017**, *56*, 13078−13082.
(8) Keppeler, M.; Bräuning, G.; Radhakrishnan, S. G.; Liu, X.; Jensen, C.; Roduner, E. Reactivity of Diatomics and of Ethylene on Zeolite-Supported 13-Atom Platinum Nanoclusters. *Catal. Sci. Technol.* **2016**, *6* (18), 6814−6823.
(9) Chen, S.; Chang, X.; Sun, G.; Zhang, T.; Xu, Y.; Wang, Y.; Pei, C.; Gong, J. Propane Dehydrogenation: Catalyst Development, New Chemistry, and Emerging Technologies. *Chem. Soc. Rev.* **2021**, *50* (5), 3315−3354.
(10) Docherty, S. R.; Rochlitz, L.; Payard, P. A.; Copéret, C. Heterogeneous Alkane Dehydrogenation Catalysts Investigated via a Surface Organometallic Chemistry Approach. *Chem. Soc. Rev.* **2021**, *50* (9), 5806−5822.
(11) Sattler, J. J. H. B.; Ruiz-Martinez, J.; Santillan-Jimenez, E.; Weckhuysen, B. M. Catalytic Dehydrogenation of Light Alkanes on Metals and Metal Oxides. *Chem. Rev.* **2014**, *114*, 10613−10653.
(12) Goodier, J. Springer Handbook of Petroleum Technology. *Ref. Rev.* **2018**, *32* (7/8), 36−36.
(13) Le Goff, P. Y.; Kostka, W.; Ross, J. *Catalytic Reforming*. Springer Handbooks; Springer, 2017; Vol. *PartF1*, pp 589−616, DOI: 10.1007/978-3-319-49347-3_18.
(14) Piccolo, L. Restructuring Effects of the Chemical Environment in Metal Nanocatalysis and Single-Atom Catalysis. *Catal. Today* **2021**, *373* (April 2020), 80−97.
(15) Batista, A. T. F.; Baaziz, W.; Taleb, A. L.; Chaniot, J.; Moreaud, M.; Legens, C.; Aguilar-Tapia, A.; Proux, O.; Hazemann, J. L.; Diehl, F.; et al. Atomic Scale Insight into the Formation, Size, and Location of Platinum Nanoparticles Supported on γ-Alumina. *ACS Catal.* **2020**, *10*, 4193−4204.
(16) Vottero, E.; Carosso, M.; Ricchebuono, A.; Jiménez-Ruiz, M.; Pellegrini, R.; Chizallet, C.; Raybaud, P.; Groppo, E.; Piovano, A. Evidence for H_2-Induced Ductility in a Pt/Al_2O_3 Catalyst. *ACS Catal.* **2022**, *12* (10), 5979−5989.
(17) Avanesian, T.; Dai, S.; Kale, M. J.; Graham, G. W.; Pan, X.; Christopher, P. Quantitative and Atomic-Scale View of CO-Induced Pt Nanoparticle Surface Reconstruction at Saturation Coverage via DFT Calculations Coupled with in Situ TEM and IR. *J. Am. Chem. Soc.* **2017**, *139* (12), 4551−4558.
(18) Sangnier, A.; Genty, E.; Iachella, M.; Sautet, P.; Raybaud, P.; Matrat, M.; Dujardin, C.; Chizallet, C. Thermokinetic and Spectroscopic Mapping of Carbon Monoxide Adsorption on Highly Dispersed $Pt/\gamma\text{-}Al_2O_3$. *ACS Catal.* **2021**, *11* (21), 13280−13293.
(19) Zhai, H.; Alexandrova, A. N. Fluxionality of Catalytic Clusters: When It Matters and How to Address It. *ACS Catal.* **2017**, *7* (3), 1905−1911.
(20) Chizallet, C.; Raybaud, P. Density Functional Theory Simulations of Complex Catalytic Materials in Reactive Environments: Beyond the Ideal Surface at Low Coverage. *Catal. Sci. Technol.* **2014**, *4* (9), 2797−2813.
(21) Hu, C. H.; Chizallet, C.; Toulhoat, H.; Raybaud, P. Structural, Energetic, and Electronic Trends in Low-Dimensional Late-Transition-Metal Systems. *Phys. Rev. B - Condens. Matter Mater. Phys.* **2009**, *79* (19), 1−11.
(22) Ellaby, T.; Aarons, J.; Varambhia, A.; Jones, L.; Nellist, P.; Ozkaya, D.; Sarwar, M.; Thompsett, D.; Skylaris, C. K. Ideal versus Real: Simulated Annealing of Experimentally Derived and Geometric Platinum Nanoparticles. *J. Phys.: Condens. Matter* **2018**, *30* (15), 155301.
(23) Van Den Bossche, M. DFTB-Assisted Global Structure Optimization of 13- and 55-Atom Late Transition Metal Clusters. *J. Phys. Chem. A* **2019**, *123* (13), 3038−3045.
(24) Yang, Q.; Jiang, G. D.; He, S. G. Enhancing the Performance of Global Optimization of Platinum Cluster Structures by Transfer Learning in a Deep Neural Network. *J. Chem. Theory Comput.* **2023**, *19* (6), 1922−1930.
(25) Raybaud, P.; Chizallet, C.; Mager-Maury, C.; Digne, M.; Toulhoat, H.; Sautet, P. From γ-Alumina to Supported Platinum Nanoclusters in Reforming Conditions: 10 Years of DFT Modeling and Beyond. *J. Catal.* **2013**, *308*, 328−340.
(26) Mager-Maury, C.; Bonnard, G.; Chizallet, C.; Sautet, P.; Raybaud, P. H_2-Induced Reconstruction of Supported Pt Clusters: Metal-Support Interaction versus Surface Hydride. *ChemCatChem.* **2011**, *3* (1), 200−207.
(27) Hu, C. H.; Chizallet, C.; Mager-Maury, C.; Corral-Valero, M.; Sautet, P.; Toulhoat, H.; Raybaud, P. Modulation of Catalyst Particle Structure upon Support Hydroxylation: Ab Initio Insights into Pd_{13} and $Pt_{13}/\gamma\text{-}Al_2O_3$. *J. Catal.* **2010**, *274* (1), 99−110.
(28) Kaiser, S.; Maleki, F.; Zhang, K.; Harbich, W.; Heiz, U.; Tosoni, S.; Lechner, B. A. J.; Pacchioni, G.; Esch, F. Cluster Catalysis with Lattice Oxygen: Tracing Oxygen Transport from a Magnetite (001) Support onto Small Pt Clusters. *ACS Catal.* **2021**, *11* (15), 9519−9529.
(29) Xu, Y.; Shelton, W. A.; Schneider, W. F. Effect of Particle Size on the Oxidizability of Platinum Clusters. *J. Phys. Chem. A* **2006**, *110* (17), 5839−5846.
(30) Laletina, S. S.; Mamatkulov, M.; Shor, E. A.; Kaichev, V. V.; Genest, A.; Yudanov, I. V.; Rösch, N. Size-Dependence of the

Adsorption Energy of CO on Pt Nanoparticles: Tracing Two Intersecting Trends by DFT Calculations. *J. Phys. Chem. C* **2017**, *121* (32), 17371−17377.
(31) Calle-Vallejo, F.; Sautet, P.; Loffreda, D. Understanding Adsorption-Induced Effects on Platinum Nanoparticles: An Energy-Decomposition Analysis. *J. Phys. Chem. Lett.* **2014**, *5* (18), 3120−3124.
(32) Grimme, S.; Schreiner, P. R. Computational Chemistry: The Fate of Current Methods and Future Challenges. *Angew. Chemie - Int. Ed.* **2018**, *57* (16), 4170−4176.
(33) Aarons, J.; Sarwar, M.; Thompsett, D.; Skylaris, C.-K. Perspective: Methods for Large-Scale Density Functional Calculations on Metallic Systems. *J. Chem. Phys.* **2016**, *145* (22), 220901.
(34) Bannwarth, C.; Caldeweyher, E.; Ehlert, S.; Hansen, A.; Pracht, P.; Seibert, J.; Spicher, S.; Grimme, S. Extended Tight-Binding Quantum Chemistry Methods. *Wiley Interdiscip. Rev. Comput. Mol. Sci.* **2021**, *11* (2), 1−49.
(35) Caldeweyher, E.; Ehlert, S.; Hansen, A.; Neugebauer, H.; Spicher, S.; Bannwarth, C.; Grimme, S. A Generally Applicable Atomic-Charge Dependent London Dispersion Correction. *J. Chem. Phys.* **2019**, *150* (15), 154122.
(36) Sarwar, M.; Cooper, C.; Briquet, L.; Ukpong, A.; Perry, C.; Jones, G. Atomic-Scale Modelling and Its Application to Catalytic Materials Science. *Johnson Matthey Technol. Rev.* **2015**, *59* (3), 257−283.
(37) Fung, V.; Jiang, D. E. Exploring Structural Diversity and Fluxionality of Pt_n (n = 10−13) Clusters from First-Principles. *J. Phys. Chem. C* **2017**, *121*, 10796−10802.
(38) Zhai, H.; Ha, M. A.; Alexandrova, A. N. AFFCK: Adaptive Force-Field-Assisted Ab Initio Coalescence Kick Method for Global Minimum Search. *J. Chem. Theory Comput.* **2015**, *11* (5), 2385−2393.
(39) Heiles, S.; Johnston, R. L. Global Optimization of Clusters Using Electronic Structure Methods. *Int. J. Quantum Chem.* **2013**, *113* (18), 2091−2109.
(40) Chang, C. M.; Chou, M. Y. Alternative Low-Symmetry Structure for 13-Atom Metal Clusters. *Phys. Rev. Lett.* **2004**, *93* (13), 1−4.
(41) Li, S.; Li, H.; Liu, J.; Xue, X.; Tian, Y.; He, H.; Jia, Y. Structural and Electronic Properties of Ru_n Clusters (n = 2−14) Studied by First-Principles Calculations. *Phys. Rev. B - Condens. Matter Mater. Phys.* **2007**, *76* (4), 1−9.
(42) Vargas, A.; Santarossa, G.; Iannuzzi, M.; Baiker, A. Fluxionality of Gold Nanoparticles Investigated by Born-Oppenheimer Molecular Dynamics. *Phys. Rev. B - Condens. Matter Mater. Phys.* **2009**, *80* (19), 1−13.
(43) Pavan, L.; Di Paola, C.; Baletto, F. Sampling the Energy Landscape of Pt_{13} with Metadynamics. *Eur. Phys. J. D* **2013**, *67*, 24.
(44) Pracht, P.; Bohle, F.; Grimme, S. Automated Exploration of the Low-Energy Chemical Space with Fast Quantum Chemical Methods. *Phys. Chem. Chem. Phys.* **2020**, *22* (14), 7169−7192.
(45) Hourahine, B.; Aradi, B.; Blum, V.; Bonafé, F.; Buccheri, A.; Camacho, C.; Cevallos, C.; Deshaye, M. Y.; Dumitric, T.; Dominguez, A.; et al. DFTB+, a Software Package for Efficient Approximate Density Functional Theory Based Atomistic Simulations. *J. Chem. Phys.* **2020**, *152* (12), 124101.
(46) Pracht, P.; Caldeweyher, E.; Ehlert, S.; Grimme, S. A Robust Non-Self-Consistent Tight-Binding Quantum Chemistry Method for Large Molecules. *ChemRxiv* **2019**, DOI: 10.26434/chemrxiv.8326202.v1.
(47) Grimme, S.; Bannwarth, C.; Shushkov, P. A Robust and Accurate Tight-Binding Quantum Chemical Method for Structures, Vibrational Frequencies, and Noncovalent Interactions of Large Molecular Systems Parametrized for All spd-Block Elements (Z = 1−86). *J. Chem. Theory Comput.* **2017**, *13* (5), 1989−2009.
(48) Bannwarth, C.; Ehlert, S.; Grimme, S. GFN2-xTB - An Accurate and Broadly Parametrized Self-Consistent Tight-Binding Quantum Chemical Method with Multipole Electrostatics and Density-Dependent Dispersion Contributions. *J. Chem. Theory Comput.* **2019**, *15* (3), 1652−1671.
(49) Senftle, T. P.; Hong, S.; Islam, M. M.; Kylasa, S. B.; Zheng, Y.; Shin, Y. K.; Junkermeier, C.; Engel-Herbert, R.; Janik, M. J.; Aktulga, H. M. The ReaxFF Reactive Force-Field: Development, Applications and Future Directions. *npj Comput. Mater.* **2016**, *2*, 15011.
(50) Van Duin, A. C. T.; Dasgupta, S.; Lorant, F.; Goddard, W. A. ReaxFF: A Reactive Force Field for Hydrocarbons. *J. Phys. Chem. A* **2001**, *105* (41), 9396−9409.
(51) Chen, Y.; Cheng, T.; Goddard, W. A. Atomistic Explanation of the Dramatically Improved Oxygen Reduction Reaction of Jagged Platinum Nanowires, 50 Times Better than Pt. *J. Am. Chem. Soc.* **2020**, *142* (19), 8625−8632.
(52) Shin, Y. K.; Gai, L.; Raman, S.; Van Duin, A. C. T. Development of a ReaxFF Reactive Force Field for the Pt-Ni Alloy Catalyst. *J. Phys. Chem. A* **2016**, *120* (41), 8044−8055.
(53) Chenoweth, K.; Van Duin, A. C. T.; Persson, P.; Cheng, M. J.; Oxgaard, J.; Goddard, W. A. Development and Application of a ReaxFF Reactive Force Field for Oxidative Dehydrogenation on Vanadium Oxide Catalysts. *J. Phys. Chem. C* **2008**, *112* (37), 14645−14654.
(54) Zou, C.; Van Duin, A. Investigation of Complex Iron Surface Catalytic Chemistry Using the ReaxFF Reactive Force Field Method. *Jom* **2012**, *64* (12), 1426−1437.
(55) Priyadarsini, A.; Mallik, B. S. Comparative First Principles-Based Molecular Dynamics Study of Catalytic Mechanism and Reaction Energetics of Water Oxidation Reaction on 2D-Surface. *J. Comput. Chem.* **2021**, *42* (16), 1138−1149.
(56) Lourenço, M. P.; Herrera, L. B.; Hostaš, J.; Calaminici, P.; Köster, A. M.; Tchagang, A.; Salahub, D. R. Automatic Structural Elucidation of Vacancies in Materials by Active Learning. *Phys. Chem. Chem. Phys.* **2022**, *24* (41), 25227−25239.
(57) O'carroll, D.; English, N. J. A DFTB-Based Molecular Dynamics Investigation of an Explicitly Solvated Anatase Nanoparticle. *Appl. Sci.* **2022**, *12* (2), 780.
(58) Liu, X.; Salahub, D. R. Molybdenum Carbide Nanocatalysts at Work in the in Situ Environment: A Density Functional Tight-Binding and Quantum Mechanical/Molecular Mechanical Study. *J. Am. Chem. Soc.* **2015**, *137* (12), 4249−4259.
(59) Spicher, S.; Bursch, M.; Grimme, S. Efficient Calculation of Small Molecule Binding in Metal-Organic Frameworks and Porous Organic Cages. *J. Phys. Chem. C* **2020**, *124* (50), 27529−27541.
(60) Pracht, P.; Grant, D. F.; Grimme, S. Comprehensive Assessment of GFN Tight-Binding and Composite Density Functional Theory Methods for Calculating Gas-Phase Infrared Spectra. *J. Chem. Theory Comput.* **2020**, *16* (11), 7044−7060.
(61) Kruse, H.; Banáš, P.; Šponer, J. Investigations of Stacked DNA Base-Pair Steps: Highly Accurate Stacking Interaction Energies, Energy Decomposition, and Many-Body Stacking Effects. *J. Chem. Theory Comput.* **2019**, *15* (1), 95−115.
(62) Cutini, M.; Bechis, I.; Corno, M.; Ugliengo, P. Balancing Cost and Accuracy in Quantum Mechanical Simulations on Collagen Protein Models. *J. Chem. Theory Comput.* **2021**, *17* (4), 2566−2574.
(63) Perdew, J. P.; Burke, K.; Ernzerhof, M. Generalized Gradient Approximation Made Simple. *Phys. Rev. Lett.* **1996**, *77* (18), 3865−3868.
(64) Steinmann, S. N.; Corminboeuf, C. Comprehensive Benchmarking of a Density-Dependent Dispersion Correction. *J. Chem. Theory Comput.* **2011**, *7* (11), 3567−3577.
(65) Kresse, G.; Hafner, J. Ab Initio Molecular-Dynamics Simulation of the Liquid-Metalamorphous- Semiconductor Transition in Germanium. *Phys. Rev. B* **1994**, *49* (20), 14251−14269.
(66) Kresse, G.; Furthmüller, J. Efficiency of Ab-Initio Total Energy Calculations for Metals and Semiconductors Using a Plane-Wave Basis Set. *Comput. Mater. Sci.* **1996**, *6* (1), 15−50.
(67) Janthon, P.; Kozlov, S. M.; Viñes, F.; Limtrakul, J.; Illas, F. Establishing the Accuracy of Broadly Used Density Functionals in Describing Bulk Properties of Transition Metals. *J. Chem. Theory Comput.* **2013**, *9* (3), 1631−1640.
(68) Vega, L.; Ruvireta, J.; Viñes, F.; Illas, F. Jacob's Ladder as Sketched by Escher: Assessing the Performance of Broadly Used

Density Functionals on Transition Metal Surface Properties. *J. Chem. Theory Comput.* **2018**, *14* (1), 395−403.
(69) Steinmann, S. N.; Corminboeuf, C. A Generalized-Gradient Approximation Exchange Hole Model for Dispersion Coefficients. *J. Chem. Phys.* **2011**, *134* (4), 044117.
(70) Gautier, S.; Steinmann, S. N.; Michel, C.; Fleurat-Lessard, P.; Sautet, P. Molecular Adsorption at Pt(111). How Accurate Are DFT Functionals? *Phys. Chem. Chem. Phys.* **2015**, *17* (43), 28921−28930.
(71) Kresse, G.; Joubert, D. From Ultrasoft Pseudopotentials to the Projector Augmented-Wave Method. *Phys. Rev. B - Condens. Matter Mater. Phys.* **1999**, *59* (3), 1758−1775.
(72) Perdew, J. P.; Ruzsinszky, A.; Csonka, G. I.; Vydrov, O. A.; Scuseria, G. E.; Constantin, L. A.; Zhou, X.; Burke, K. Restoring the Density-Gradient Expansion for Exchange in Solids and Surfaces. *Phys. Rev. Lett.* **2008**, *100* (13), 1−4.
(73) Gale, J. D.; Rohl, A. L. The General Utility Lattice Program (GULP). *Mol. Simul.* **2003**, *29* (5), 291−341.
(74) Sanz-Navarro, C. F.; Astrand, P.-O.; Chen, D.; Rønning, M.; van Duin, A. C. T.; Jacob, T.; Goddard, W. A. Molecular Dynamics Simulations of the Interactions between Platinum Clusters and Carbon Platelets. *J. Phys. Chem. A* **2008**, *112* (7), 1392−1402.
(75) McDouall, J. J. W. *Computational Quantum Chemistry: Molecular Structure and Properties in Silico*; RSC theoretical and computational chemistry series; RSC Publishing, 2013.
(76) Nosé, S. An Extension of the Canonical Ensemble Molecular Dynamics Method. *Mol. Phys.* **1986**, *57*, 187−191.
(77) Berendsen, H. J. C.; Postma, J. P. M.; Van Gunsteren, W. F.; Dinola, A.; Haak, J. R. Molecular Dynamics with Coupling to an External Bath. *J. Chem. Phys.* **1984**, *81* (8), 3684−3690.
(78) Lambie, S. G.; Weal, G. R.; Blackmore, C. E.; Palmer, R. E.; Garden, A. L. Contrasting Motif Preferences of Platinum and Gold Nanoclusters between 55 and 309 Atoms. *Nanoscale Adv.* **2019**, *1* (6), 2416−2425.
(79) Momma, K.; Izumi, F. VESTA3 for Three-Dimensional Visualization of Crystal, Volumetric and Morphology Data. *J. Appl. Crystallogr.* **2011**, *44* (6), 1272−1276.
(80) Humphrey, W.; Dalke, A.; Schulten, K. VMD: Visual Molecular Dynamics. *J. Mol. Graph.* **1996**, *14* (1), 33−38.
(81) Waskom, M. Seaborn: Statistical Data Visualization. *J. Open Source Softw.* **2021**, *6* (60), 3021.
(82) Li, L.; Larsen, A. H.; Romero, N. A.; Morozov, V. A.; Glinsvad, C.; Abild-Pedersen, F.; Greeley, J.; Jacobsen, K. W.; Nørskov, J. K. Investigation of Catalytic Finite-Size-Effects of Platinum Metal Clusters. *J. Phys. Chem. Lett.* **2013**, *4* (1), 222−226.
(83) McQuarrie, D. A.; Simon, J. D. *Physical Chemistry: A Molecular Approach*; University Science Books: Sausalito, CA, 1997.

https://doi.org/10.1021/acs.jpcc.3c02799
J. Phys. Chem. C 2023, 127, 18454−18465